ISCI, Volume *19*

Supplemental Information

Quasi-Metal for Highly Sensitive and Stable Surface-Enhanced Raman Scattering

Zheng Tian, Hua Bai, Chao Chen, Yuting Ye, Qinghong Kong, Yahui Li, Wenhao Fan, Wencai Yi, and Guangcheng Xi

Supplemental Information

1. Transparent Methods

Synthesis of b-VO_2 nanosheets

All chemicals used in the experiments are of analytical purity. In a typical synthesis, 0.1 g of vanadyl acetylacetonate (VAA) is dissolved in 30 mL of absolute ethanol to form a bright blue transparent solution. The resulting homogeneous solution is then transferred to a Teflon-lined high-pressure reactor, and a common glass sheet is placed above the liquid level as a growth platform for b-VO_2 nanosheets. The Teflon-lined stainless steel autoclave was sealed and heated for 20 h at 200 °C. After the reaction is completed, the glass sheet covered with black products was taken out. Finally, the black glass was washed with ethanol and distilled water for three times and dried at 50 °C in a vacuum drying oven.

Synthesis of SiO_2/VO_2

Open a bottle of analytically pure silicon tetrachloride ($SiCl_4$) in air. Soon, a lot of "white-fog" formed at the mouth of the bottle. Place the glass sheet covered with VO_2 nanosheets in a white mist at the mouth of the bottle for 3 min. Then, the glass sheet is placed in a nitrogen-protected tubular furnace and heated to 400 °C for 1 hours. After natural cooling, take out for use.

Synthesis of urchin-like $W_{18}O_{49}$ nanostructures

In a typical procedure, 3 g of WCl_6 was dissolved in 100 mL of ethanol, and the obtained yellow solution was magnetically stirred for 20 min, and then transferred to a Teflon-lined stainless-steel autoclave and heated at 200 °C for 20 h with a heating rate

of 4 °C/min. The autoclave was cool down naturally and a blue product was collected, washed, and dried in a vacuum drying oven at 50 °C for 4 h.

Characterization

These samples were measured by a variety of characterization techniques. XRD patterns of the products were obtained on a Bruker D8 focus X-ray diffractometer by using CuKa radiation (λ = 1.54178 Å). SEM images and EDS were obtained on a Hitachi S-4800. TEM and HRTEM characterizations were performed with a Tecnai G F30 operated at 300 kV. Ultraviolet–Vis (UV) absorption spectra were recorded with a Shimadzu UV3600. XPS were recorded on an ESCALab-250Xi of ThermoFisher Scientific. The Fourier transform infrared spectra were measured from THERMO Iz-10. The specific surface area was measured in a Micro Tristar II 3020. The work functions of b-VO_2 nanosheets was detected from Kelvin probe force microscope, Multimode-Picoforce-Veeco. ESR spectrum was obtained from ESP-300.

Raman tests

To study the SERS of these b-VO_2 nanosheets, a confocal micro Raman spectrometer (Renishaw-inVia Reflex) is used as the measuring instrument. In all SERS tests, unless specifically stated, the excitation wavelength is 532 nm, laser power is 0.5 mW and the specification of the objective is × 50 L. A series of standard solution (aqueous) of highly risk chemical with concentrations of 10^{-7}-10^{-10} M were used as the probe molecules. To improve the signal reproducibility and uniformity, before each test, the glass sheet (1 cm × 1 cm) covered with b-VO_2 nanosheets were immersed into a 20 mL of probe solution with specific concentration for 20 min, then taken out and dried

in air for 20 min. In all SERS tests, the laser beam is perpendicular to the top of the sample to be tested with a resultant beam spot diameter of 5 μm. The calculation of EF are provided in Supplementary Methods.

Enhanced Factor Calculation

To calculate the EF of the b-VO_2 nanosheets, the ratio of SERS to normal Raman spectra (NRS) of RH6G was determined by using the following calculating formula 1

$$EF = (I_{SERS}/I_{NRS}) \times (C_{NRS}/C_{SERS}) \quad (1)$$

where I_{SERS} and I_{NRS} refer to the peak intensities of the SERS and NRS, respectively. C_{NRS} and C_{SERS} refer to the concentrations of the probe molecules of the NRS and SERS, respectively. In the SERS measurements, two Raman scattering peaks, R_1 at 612 cm^{-1} and R_2 at 773 cm^{-1} were selected for the calculations of the EF. For comparison, the peak intensities of the R6G (1×10^{-2} M, aqueous solution) directly placed on bare glass slide were detected as NRS data. For the NRS data, the integration time is 4000 s, while for the SERS data, the integration time is 10 s.

Calculations details

All the density functional theory (DFT) calculations were carried out using the Vienna Ab initio Simulation Package (VASP)[1-3]. The Perdew-Burke-Ernzerhof (PBE) was used to describe the exchange-correlation[4]. The optimization process was performed using a conjugate gradient algorithm with a force tolerance of 0.02 eV/Å, with kinetic energy cutoff set as 500 eV. A Gamma k-point sampling of 3 × 7 × 5 was used to optimize the VO_2 cell parameters. The optimized lattice parameters were 11.99, 3.74, 6.40 Å, and 90.0, 107.0, 90.0°, respectively.

To calculate the VO_2 (112) surface, a $2 \times 2 \times 1$ supercell was built by cut the original cell along (112) facet, with a 20 Å additional vacuum layer in z-direction. Thus, the lattice parameter of the layer slab model was 24.82 Å × 19.68 Å × 26.97 Å. A 2D-shaped graphene layer was calculated to adsorb RH6G molecule as well, containing 200 carbon atoms, with the supercell parameters equal to 24.47 Å × 24.67 Å × 20 Å and 90, 90, 120°, respectively. The structure of RH6G molecule was optimized in the same cell as well. For these simulations, the plane wave cutoff energy set as 500 eV and the k-point mesh set as 1 × 1 × 1.

1. Kresse, G., and Hafner, J. (1994). Ab initio molecular-dynamics simulation of the liquid-metal–amorphous-semiconductor transition in germanium. Phys. Rev. B *49*, 14251-14269 .

2. Kresse, G., and Furthmüller, J. (1996). Efficiency of ab-initio total energy calculations for metals and semiconductors using a plane-wave basis set. J. Comp. Mater. Sci. *6*, 15-50.

3. Kresse, G., and Furthmüller, (1996). J. Efficient iterative schemes for ab initio total-energy calculations using a plane-wave basis set. Phys. Rev. B *54*, 11169-11186.

4. Perdew, J. P., Burke, K., and Ernzerhof, M. (1996). Generalized gradient approximation made simple. Phys. Rev. Lett. *77*, 3865-3868 .

2. Supporting Figures

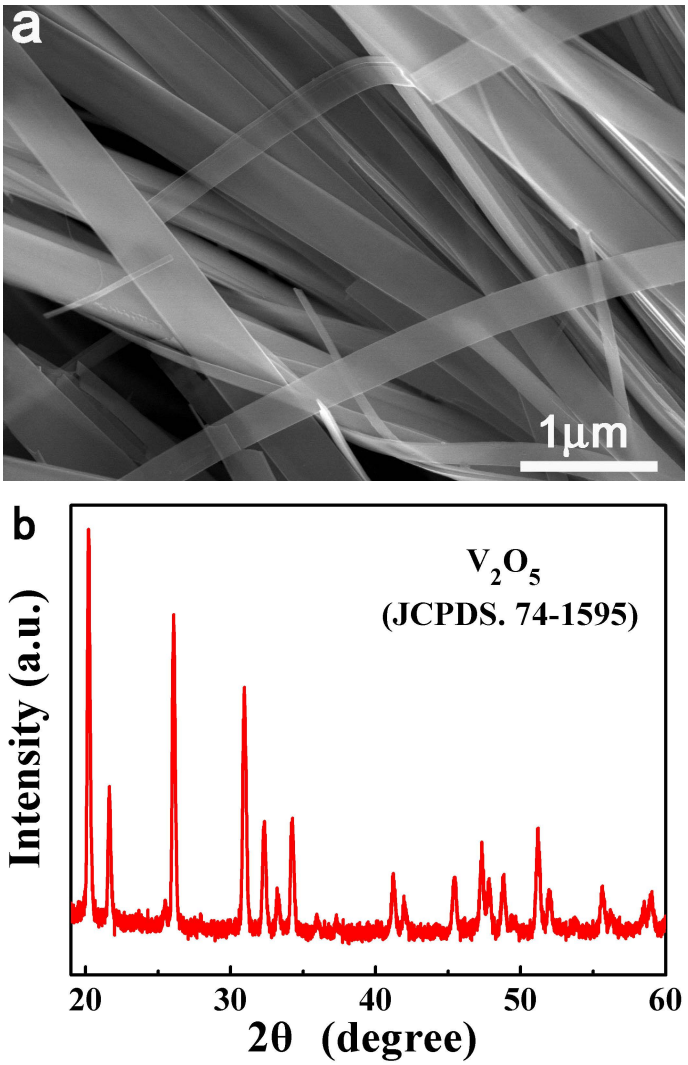

Figure S1. SEM image (a) and XRD pattern (b) of the V_2O_5 nanobelts obtained when ethanol is replaced by deionized water. Related to Figure 1.

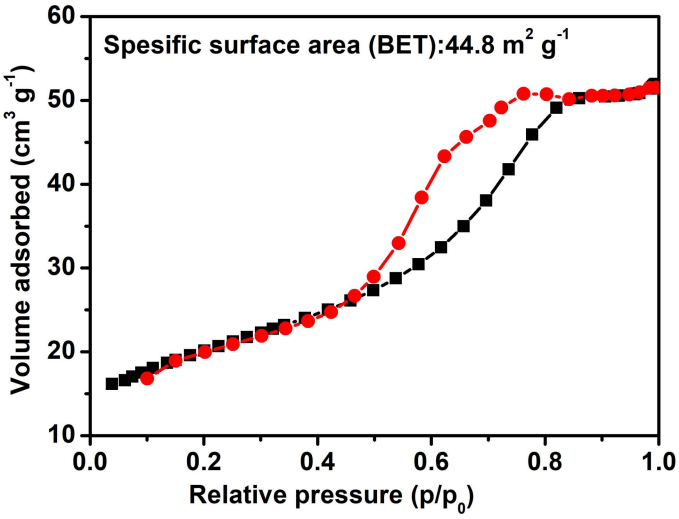

Figure S2. N_2 adsorption/desorption isotherms of the as-synthesized b-VO_2 nanosheets, related to Figure 1.

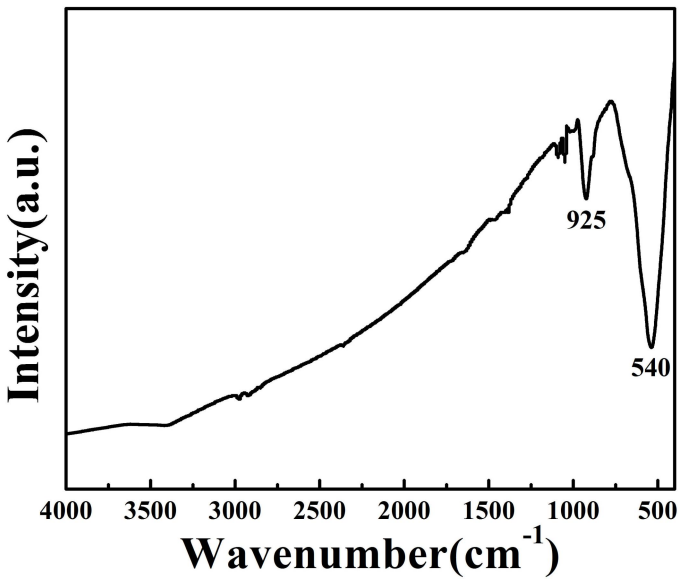

Figure S3. FTIR spectrum of the as-synthesized b-VO_2 nanosheets, related to Figure 1.

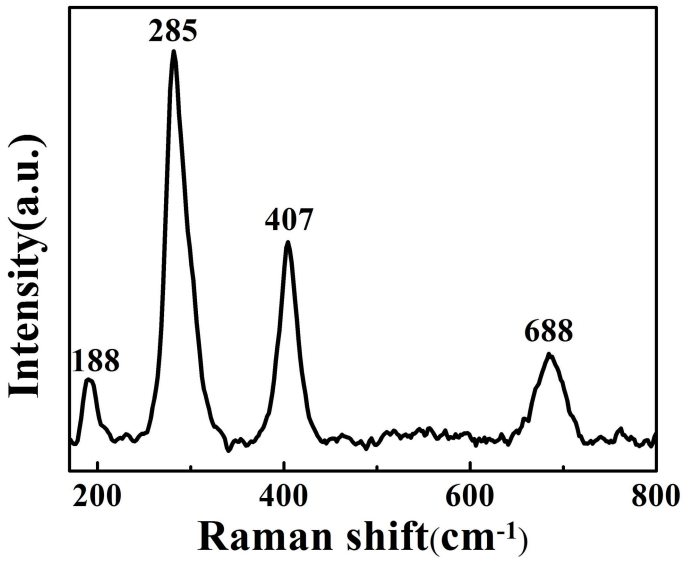

Figure S4. Raman spectrum of the b-VO_2 nanosheets, related to Figure 1.

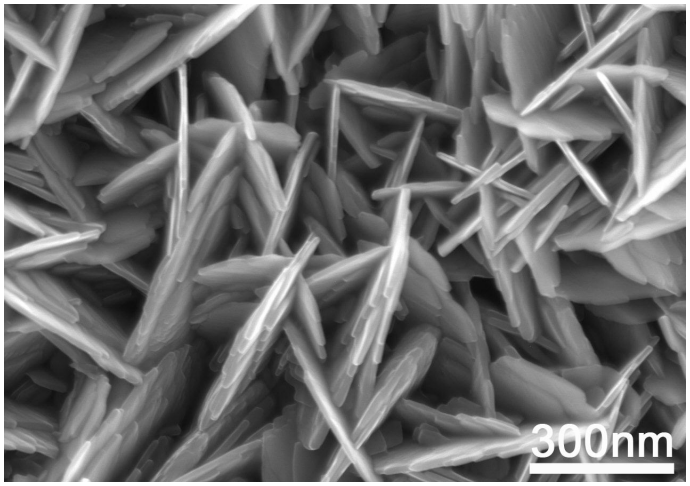

Figure S5. TEM image of the V_2O_5 nanosheets prepared by heating the b-VO_2 nanosheets at 400 °C, related to Figure 2.

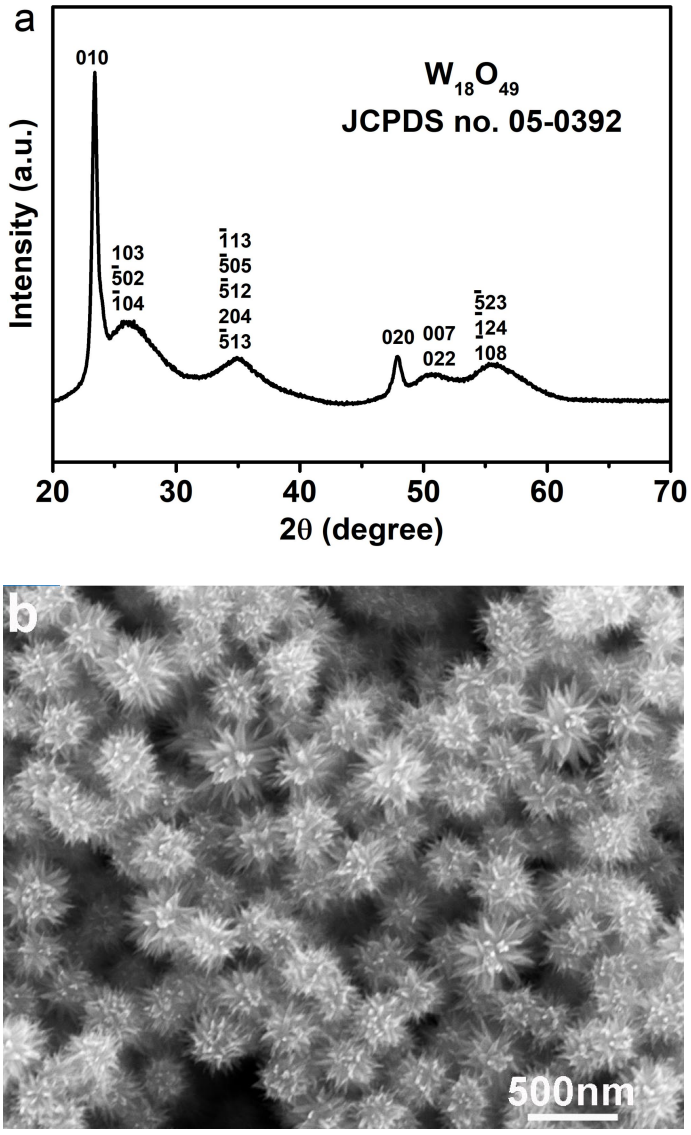

Figure S6. XRD pattern (a) and SEM image (b) of the prepared urchin-like $W_{18}O_{49}$ nanostructures. Related to Figure 2.

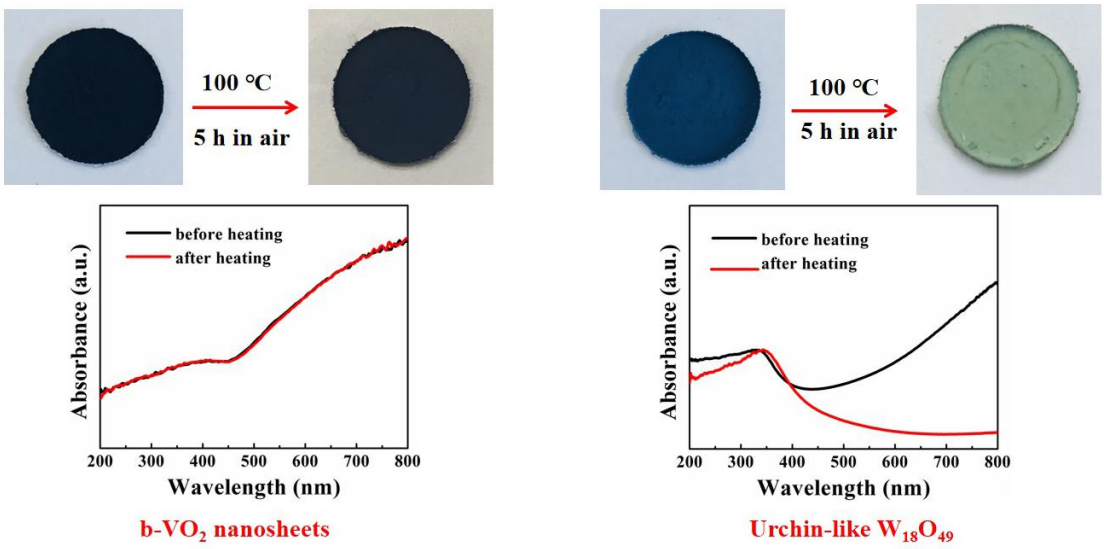

Figure S7. The comparison of oxidation resistance between b-VO_2 and $W_{18}O_{49}$. The change of color and absorbance before and after heating from two kinds of samples clearly indicated that the oxidation resistance of $W_{18}O_{49}$ is much lower than that of b-VO_2. Related to Figure 2.

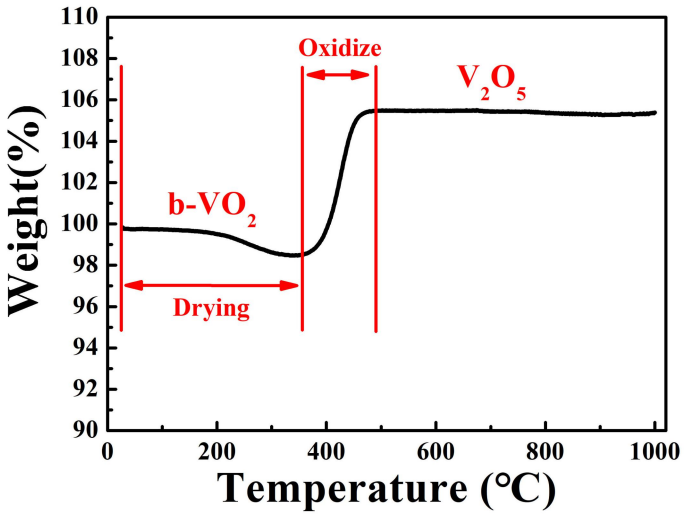

Figure S8. The differential thermal analysis (DTA) curve of the b-VO_2 nanosheets. Below 350 °C, the b-VO_2 nanosheets are stable. When the temperature continues to rise, they were gradually oxidized to V_2O_5. Related to Figure 2.

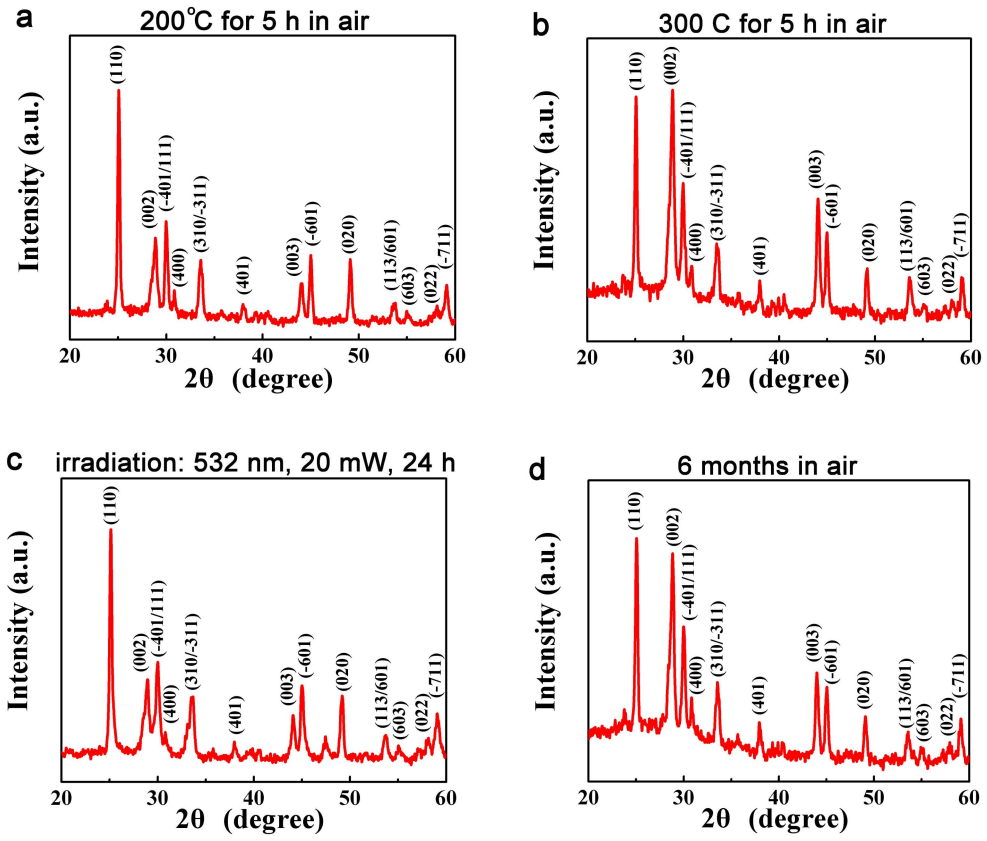

Figure S9. A series of XRD patterns demonstrated that no detectable change in the XRD patterns of b-VO_2 nanosheets after the heating, irradiating, and long-term storage. Related to Figure 2.

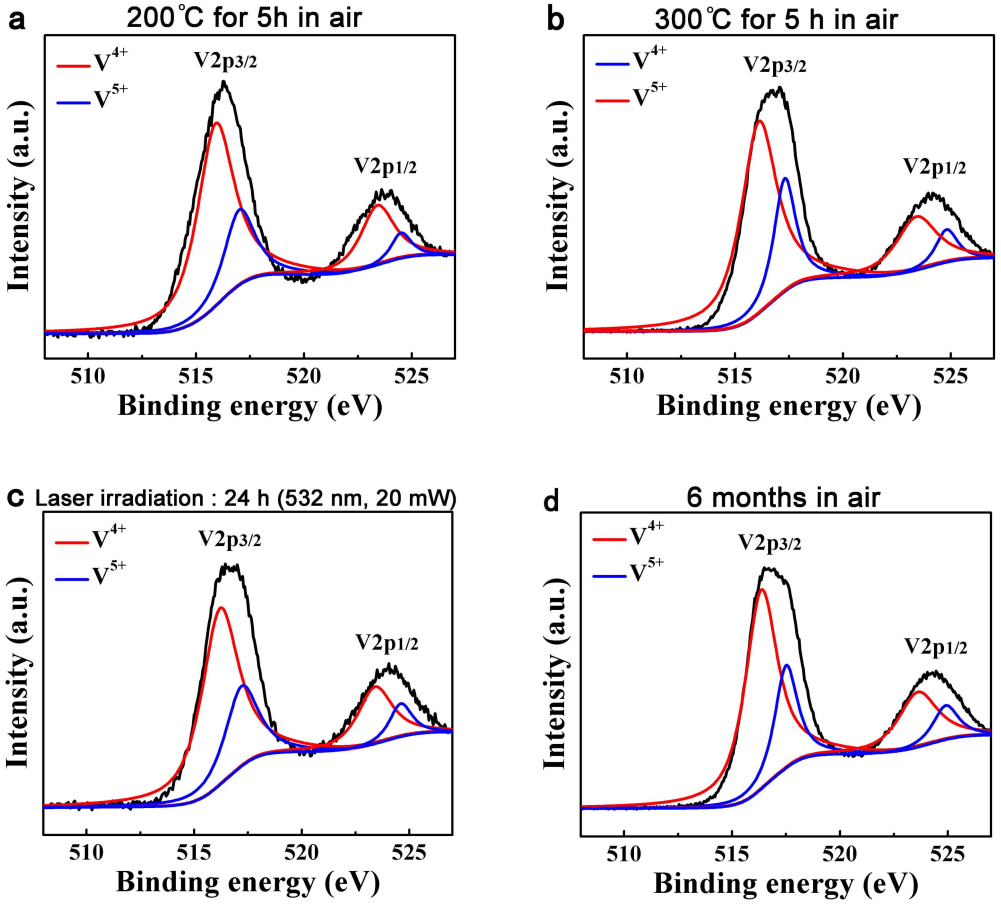

Figure S10. A series of XPS spectra demonstrated that no detectable change in the valence state of the b-VO_2 nanosheets after the heating, irradiation, and long-term storage. The XPS and XRD (Figure S6) results demonstrate that the stability of these b-VO_2 nanosheets is extraordinary high. Related to Figure 2.

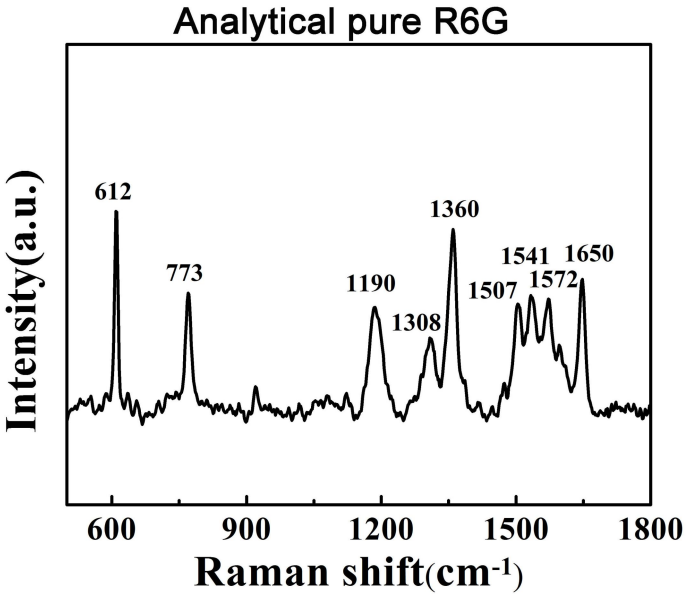

Figure S11. The standard Raman spectrum of R6G reference material, related to Figure 3.

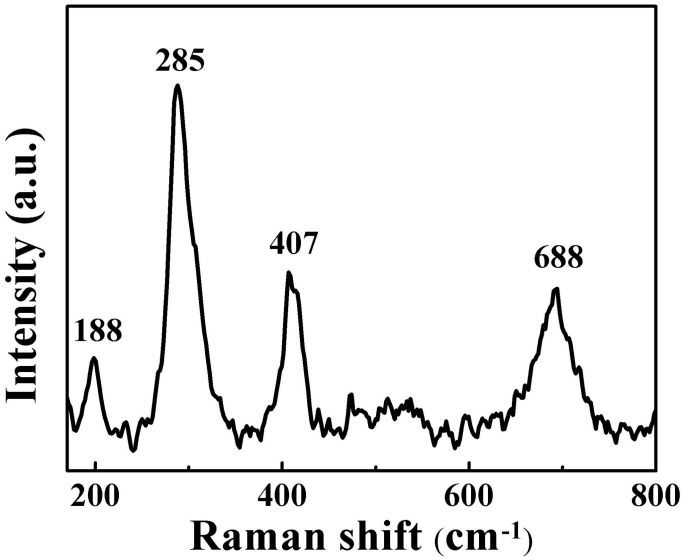

Figure S12. The bare b-VO_2 nanosheet arrays without R6G solution only showed the typical Raman scattering peaks of themself, related to Figure 3.

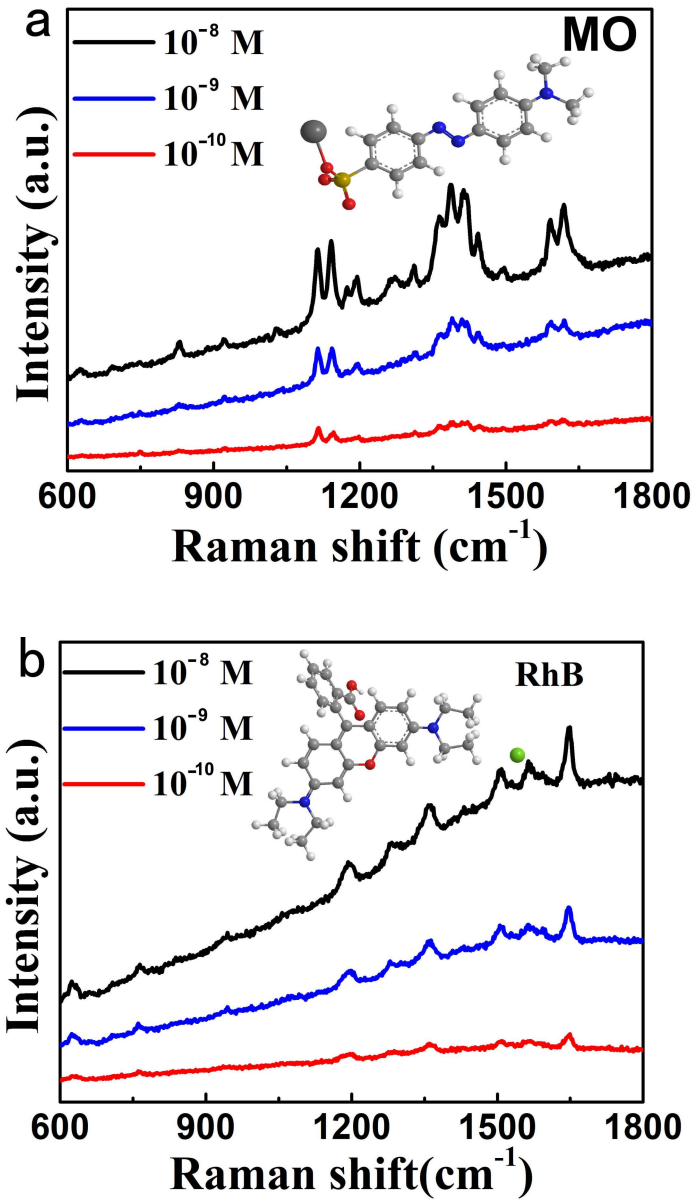

Figure 13. SERS spectra of the dye molecules of MO (a) and RhB (b). Related to Figure 3.

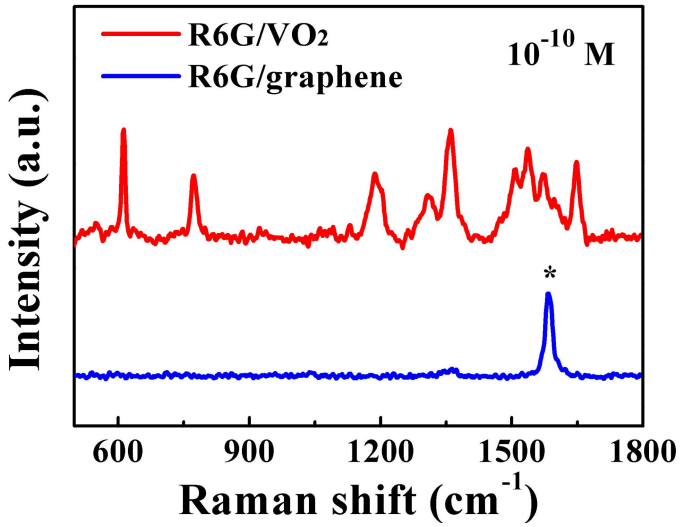

Figure S14. SERS spectra of 10^{-10} M R6G on b-VO_2 nanosheets and graphene, respectively, related to Figure 6.

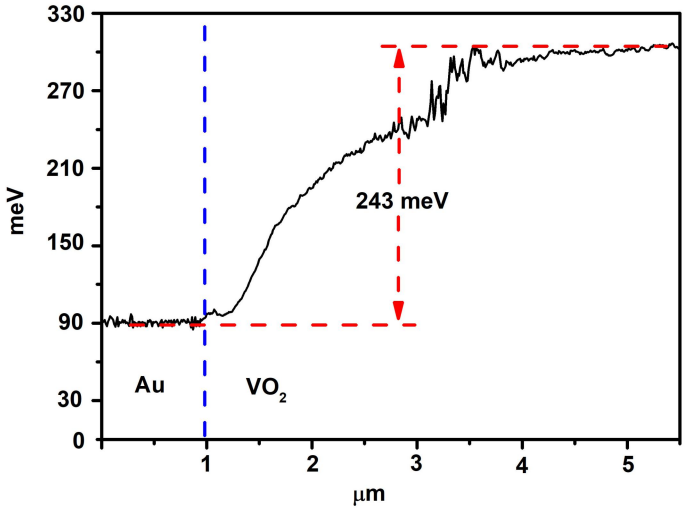

Figure S15. The measured surface potential difference profiles. Considering that the work function of Au reference is 4.8 eV, the work function of b-VO_2 nanosheets is estimated to be 4.55 eV. The b-VO_2 thickness dependence on its work function can be neglected. Related to Figure 6.

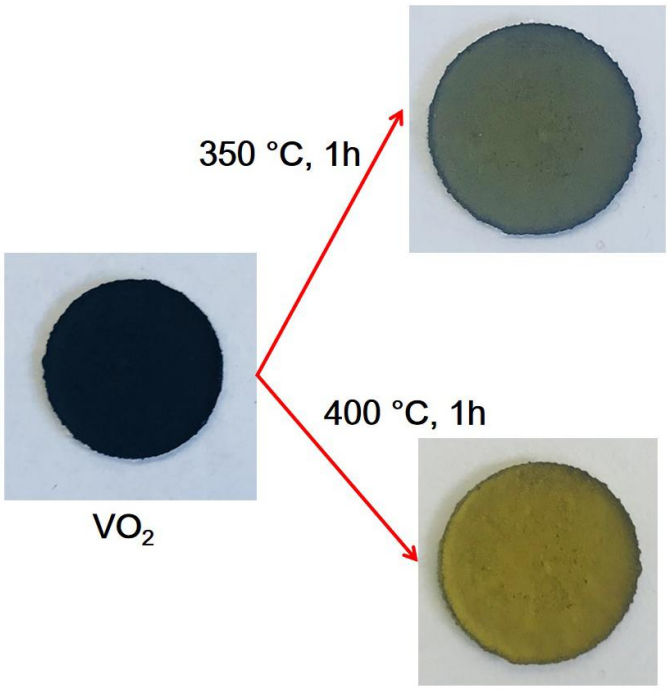

Figure S16. When these b-VO_2 nanosheets were heated in air for a period of time, their colors have changed dramatically. Related to Figure 6.

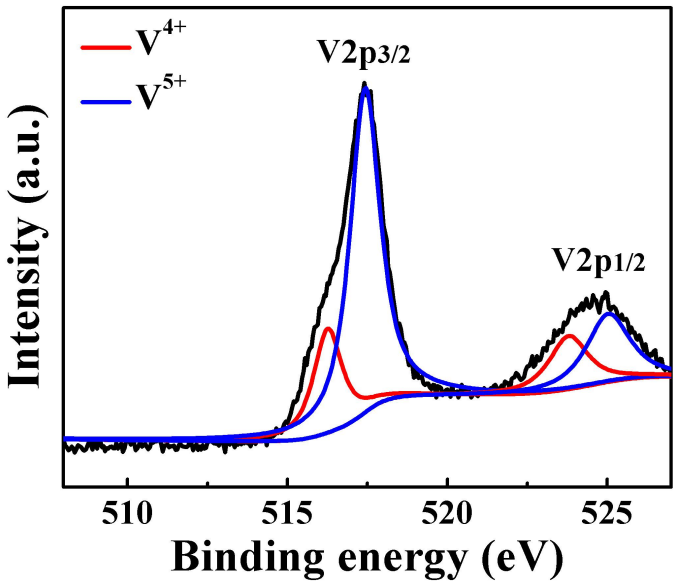

Figure S17. The XPS spectrum of the sample after heating at 400 °C for 1h in air, which suggests that the VO_2 has been transformed into V_2O_5. Related to Figure 6.

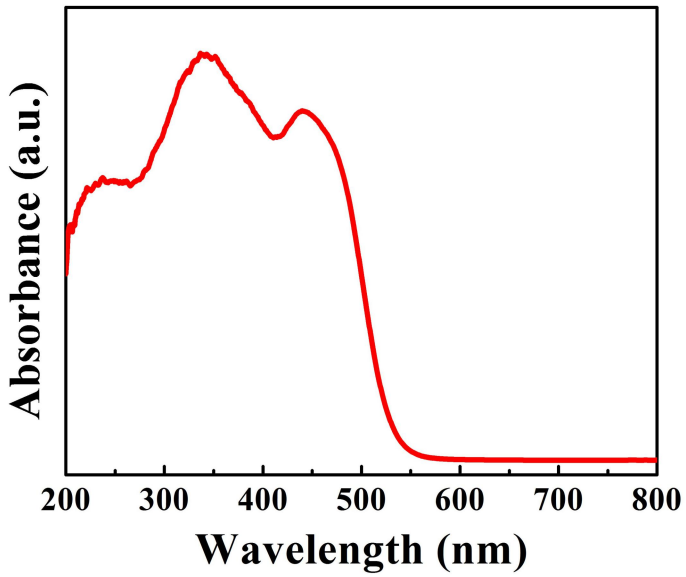

Figure S18. The UV-Vis absorption of the sample after heating at 400 °C for 1h in air, related to Figure 6.

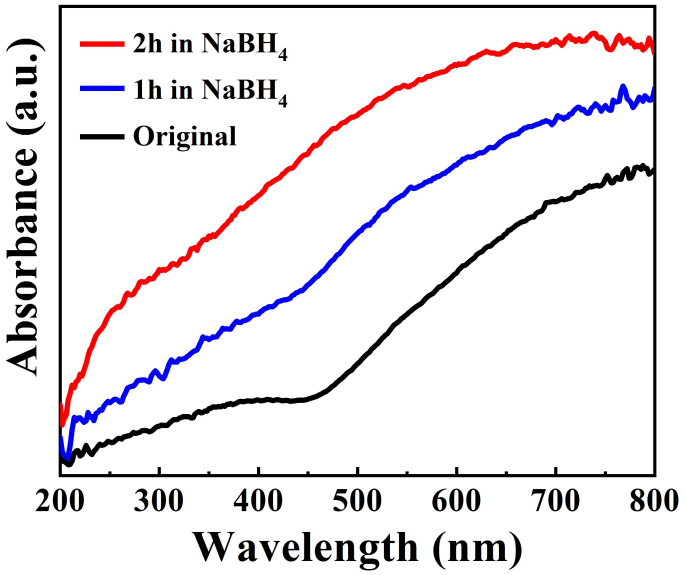

Figure 19. The UV-Vis absorption of the VO_2 samples reduced by $NaBH_4$ aqueous solution, related to Figure 6.

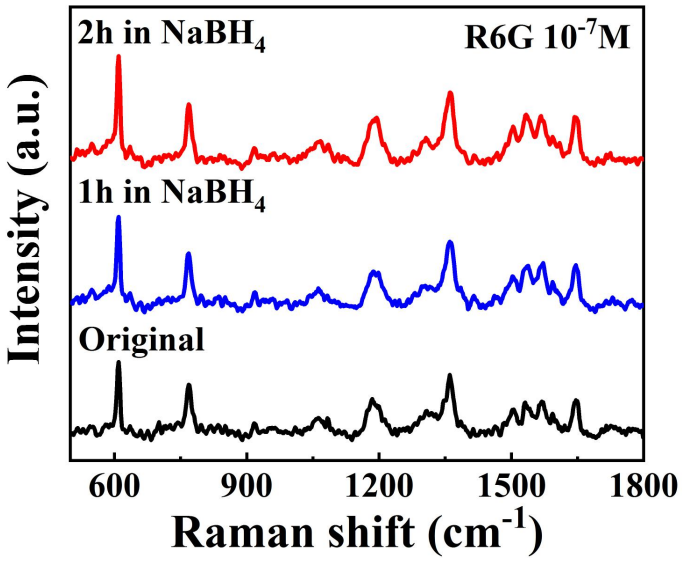

Figure S20. The obtained SERS signals from the reduced VO_2 nanosheet substrates, related to Figure 6.

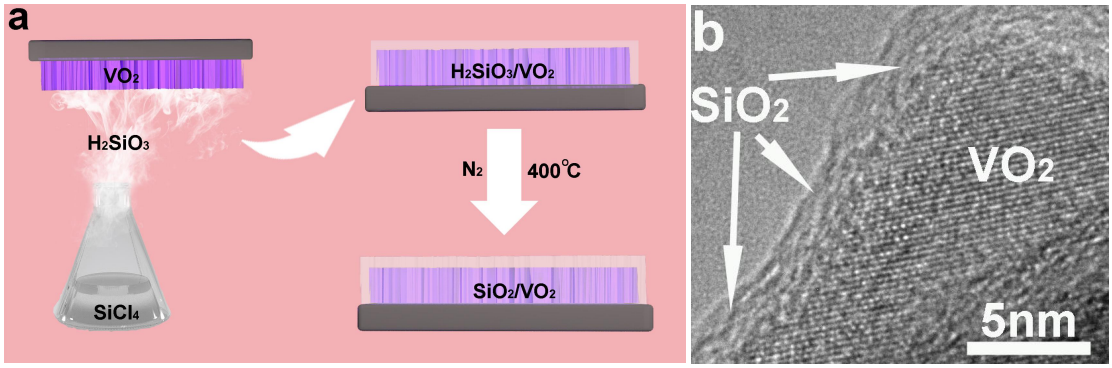

Figure 21. (a) Schematic illustrating the synthesis of the SiO_2/VO_2. $SiCl_4$ is easily hydrolyzed into H_2SiO_3 in air. These formed H_2SiO_3 species were coated on VO_2 nanosheets and formed H_2SiO_3/VO_2. The VO_2 nanosheets coated with amorphous SiO_2 layers were obtained by heating under N_2 protection. (b) The HRTEM image of the obtained SiO_2/VO_2, revealing the thickness of SiO_2 layer is about 2 nm. Related to Figure 6.

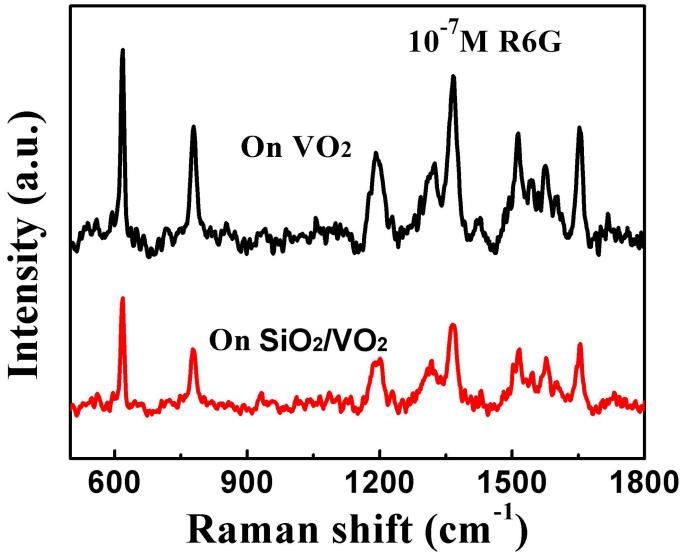

Figure S22. (a) The obtained SERS signals from VO_2 nanosheet substrate and SiO_2/VO_2 substrate, respectively. Related to Figure 6.

Table S1: Some of the previously reported EFs for Non-Noble Metal Enhanced Raman Substrate materials, related to Figure 3

Substrate	Probe molecule	Excited wavelength (nm)	Author	EF	Detectable Limit (M)	Stability
TiO_2	MB	532	D. Qi et al., 2014	2×10^4	10^{-5}	stable
CdTe	4-Mpy	514.5	Y. F. Wang et al., 2007	10^4	10^{-3}	Liable to oxidation and corrosion
ZnO	D266	488	H. Wen et al., 1996	50	10^{-5}	Liable to corrosion
CdS	4-Mpy	514.5	Y. F. Wang et al., 2008	10^2	10^{-3}	Liable to oxidation and corrosion
α -Fe_2O_3	4-Mpy	514.5	X. Q. Fu et al., 2009	2.7×10^4	10^{-3}	Liable to corrosion
Cu_2O	4-MBA	488	L. Jiang et al., 2013	10^5	10^{-3}	Liable to oxidation and corrosion
CuO	4-Mpy	514.5	Y. Wang et al., 2007	10^2	10^{-1}	Liable to corrosion
$W_{18}O_{49}$	R6G	532.8	S. Cong et al., 2015	3.4×10^5	10^{-7}	Liable to oxidation
Cu_2O	R6G	532	L. Guo et al., 2017	8×10^5	10^{-9}	Liable to oxidation and corrosion
ZnO	4-MBA	633	Wang, X. T. et al., 2017	6.6×10^5		Liable to corrosion
MoS_2	R6G	532.8	Zheng, Z. H. et al., 2017	1.6×10^5	10^{-7}	Liable to oxidation
						Liable to

MOF	R6G	532.8	Sun, H. Z. et al., 2019	10^6	10^{-8}	oxidation and corrosion
Organic Semiconductor	DFH-4T	532	Yilmaz M. et al., 2017	3.4×10^3	10^{-5}	Liable to oxidation and corrosion
Nb_2O_5	MB	532	Shan, Y. F. et al., 2017	7.1×10^6	10^{-9}	stable
WTe_2/WTe_2	R6G	532	Tao, L. et al., 2018	6.2×10^9	10^{-15}	Liable to oxidation and corrosion
MoO_2	R6G	532	Zhang, Q. et al., 2017	3.75×10^6	10^{-7}	stable
b-VO_2	**R6G**	**532**	**Tian, Z. et al (this work)**	**6.7×10^7**	**10^{-10}**	stable

Qi, D., Lu, L., Wang, L., and Zhang, J. (2014). Improved SERS sensitivity on plasmon-free TiO_2 photonic microarray by enhancing light-matter coupling. J. Am. Chem. Soc. *136*, 9886–9889.

Wang, Y. F., Suna, Z. H., Wanga, Y. X., Hua, H. L., Zhaoa, B., Xua, W. Q., and Lombardi, G. R. (2007). Surface-enhanced Raman scattering on mercaptopyridine-capped CdS microclusters. Spectrochim. Acta, Part A. *66*, 1199–1203.

Wen, H., He, T. J., Xu, C. Y., Zuo, J., and Liu, F. C. (1996). Surface enhancement of Raman and absorption spectra from cyanine dye D266 adsorbed on ZnO colloids. Molecular Physics. *88*, 281–290.

Wang, Y. F., Zhang, J. H., Jia, H. Y., Li, M. J., Zeng, J. B., Yang, B., Zhao, B., and Xu, W. Q. (2008). Mercaptopyridine surface-functionalized CdTe quantum dots with

enhanced Raman scattering properties. J. Phys. Chem. C. *112*, 996–1000.

Fu, X. Q., Bei, F. L., Wang, X., Yang, X. J., and Lu, L. D. (2009). Surface-enhanced Raman scattering of 4-mercaptopyridine on sub-monolayers of α-Fe_2O_3 nanocrystals (sphere, spindle, cube). J. Raman Spectrosc. *40*, 1290–1295.

Jiang, L.,You, T. T., Yin, P. J., Shang, Y., Zhang, D. F., Guo, L., and Yang, S. (2013). Surface-enhanced Raman scattering spectra of adsorbates on Cu_2O nanospheres: charge-transfer and electromagnetic enhancement. Nanoscale. *5*, 2784–2789.

Wang, Y., Hu, H. L., Jing, S. Y., Wang, Y. X., Sun, Z. H., Zhao, B., Zhao, C., and Lombardi, J. R. (2007). Enhanced Raman scattering as a probe for 4-mercaptopyridinesurface-modified copper oxide nanocrystals. Anal. Sci. *23*, 787–791.

Cong, S., Yuan1, Y. Y., Chen, Z. G., Hou, J. Y., Yang, M., Su, Y. L., Zhang, Y. Y., Li, L., Li, Q. W., Geng, F. X., and Zhao, Z. G. (2015). Noble metal-comparable SERS enhancement from semiconducting metal oxides by making oxygen vacancies. Nat. Commun. *6*, 7800.

Lin, J., Shang, Y., Li, X. X., Yu, J., Wang, X. T., and Guo L. (2017). Ultrasensitive SERS detection by defect engineering on single Cu_2O superstructure particle. Adv. Mater. *29*, 1604797.

Guo, L., Wang, X. T., Shi, W. X., Jin, Z., Huang, W. F., Lin, J., Ma, G. S., and Li, S. Z. (2017). Remarkable SERS activity observed from amorphous ZnO nanocages. Angew. Chem. Int. Ed. *56*, 9851–9855.

Zheng, Z. H., Cong, S., Gong, W. B., Xuan, J. N., Li, G. H., Lu, W. B., Geng F. X.,

and Zhao Z. G. (2017). Semiconductor SERS enhancement enabled by oxygen incorporation. Nat. Commun. *8*, 1993.

Sun, H. Z., Cong, S., Zheng, Z. H., Wang, Z., Chen, Z. G., and Zhao, Z. G. (2019). Metal–organic frameworks as surface enhanced Raman scattering substrates with high tailorability. J. Am. Chem. Soc. *141*, 870–878.

Yilmaz, M., Babur, E., Ozdemir, M., Gieseking, R. L., Dede, Y., Tamer, U., Schatz, G. C., Facchetti, A., Usta, H., and Demirel, G. (2017). Nanostructured organic semiconductor films for molecular detection with surface-enhanced Raman spectroscopy. Nat. Mater. *16*, 918–924.

Shan, Y. F., Zheng, Z. H., Liu, J. J., Yang, Y., Li, Z. Y., Huang, Z. R., and Jiang D. L. (2017). Niobium pentoxide: a promising surface-enhanced Raman scattering active semiconductor substrate. npj Comput. Mater. *3*, 11.

Li, T., Chen, K., Chen, Z. F., Cong, C. X., Qiu, C. Y., Chen, J. J., Wang, X. M., Chen, H. J., Yu, T., Xie, W. J., et al. (2018). 1T' transition metal telluride atomic Layers for plasmon-free SERS at femtomolar levels. J. Am. Chem. Soc. *140*, 8696–8704.

Zhang, Q. Q., Li, X. S., Ma, Q., Zhang, Q., Bai, H., Yi, W. C., Liu, J. Y., Han, J., and Xi, G. C. (2017). A metallic molybdenum dioxide with high stability for surface enhanced Raman spectroscopy. Nat. Commun. *8*, 14903.